Optimizing ExoMars 2022 Rover Remote Sensing Multispectral Science: Cross-Rover Comparison using Laboratory and Orbital Data

P. M. Grindrod[1], R. B. Stabbins[1], S. Motaghian[1], E. J. Allender[2], C. R. Cousins[2], M. S. Rice[3], and K. Stephan[4]

[1] *Department of Earth Sciences, Natural History Museum, London, UK*

[2] *School of Earth & Environmental Sciences, University of St Andrews, UK.*

[3] *Department of Geology, Western Washington University, WA, USA.*

[4] *Deutsches Zentrum für Luft- und Raumfahrt (DLR), Berlin, Germany.*

Corresponding Author

Peter Grindrod

Department of Earth Sciences, Natural History Museum, London, SW7 5BD, UK.

Email: p.grindrod@nhm.ac.uk

ORCID: 0000-0002-0934-5131

Abstract

Multispectral imaging instruments have been core payload components of Mars lander and rover missions for several decades. In order to place into context the future performance of the ExoMars 2022 Rosalind Franklin rover, we have carried out a detailed analysis of the spectral performance of three visible and near-infrared (VNIR) multispectral instruments. We have determined the root mean square error (RMSE) between the expected multispectral sampling of the instruments and high-resolution spectral reflectance data, using both laboratory spectral libraries and Mars orbital hyperspectral data. ExoMars Panoramic Camera (PanCam) and Mars2020 Perseverance Mastcam-Z instruments have similar values of RMSE, and are consistently lower than for Mars Science Laboratory Mastcam, across both laboratory and orbital remote sensing data sets. The performance across mineral groups is similar across all instruments, with the lowest RMSE values for hematite, basalt, and basaltic soil. Minerals with broader, or absent, absorption features in these visible wavelengths, such as olivine, saponite, and vermiculite have overall larger RMSE values. Instrument RMSE as a function of filter wavelength and bandwidth suggests that spectral parameters that use shorter wavelengths are likely to perform better. Our simulations of the spectral performance of the PanCam instrument will allow the future use of targeted filter selection during ExoMars 2022 Rosalind Franklin operations on Mars.

Plain Language Summary

Mars landers and rovers tend to carry camera instruments that record images at a range of different wavelengths. Such multispectral instruments can be used

to help determine the composition of the surface, and guide both scientific analyses and mission operations. Subtle differences in the exact wavelengths that are sampled on different instruments mean that comparison across missions is not straightforward. In this study we simulate the performance of three different multispectral camera instruments: ExoMars Panoramic Camera (PanCam), Mars Science Laboratory Mastcam, and Mars2020 Perseverance Mastcam-Z. We compare the ability of each instrument to determine the true spectral response for both laboratory data compiled into spectral libraries, and for hyperspectral data recorded of the surface of Mars. We find that the choice of filters for PanCam and Mastcam-Z result in similar performance between these two instruments, with both apparently performing better than Mastcam. This study will allow more confident comparison of results from across instruments, and help the development of best practice for the future use of the ExoMars PanCam instrument.

1. Introduction

The scientific objectives of the ExoMars 2022 Rosalind Franklin rover mission, due to land on Mars in 2023, are to (1) search for signs of past and present life on Mars, and (2) to characterize the geochemical environment as a function of depth in the shallow subsurface (*Vago et al.*, 2015; *Vago et al.*, 2017). The primary remote sensing instrument on previous Mars landers and rovers has been multispectral imagers operating in the visible and near-infrared (VNIR) wavelengths (e.g. *Bell et al.*, 2019; *Gunn and Cousins*, 2016). In addition to allowing geomorphological interpretations of the surface, the acquisition of in situ spectral information can help determine the composition of the environment close to the lander or rover. Although diagnostic spectral features of planetary surfaces tend to occur at longer IR wavelengths (e.g. *Clark*, 2019; *Mustard and Glotch*, 2019; *Rossman and Ehlmann*, 2019), there are many examples of studies using VNIR multispectral imaging instruments to derive important compositional information about both crystalline and amorphous materials (e.g. *Farrand et al.*, 2019), which not only allow deeper scientific investigations (e.g. *Fraeman et al.*, 2020; *Horgan et al.*, 2020; *Wellington et al.*, 2017), but also have an impact on tactical and strategic planning during mission operations (e.g. *Squyres et al.*, 2008). Such studies have ranged in their scope, including, but not limited to soil composition with Mars Pathfinder (*Bell III et al.*, 2000), rock coatings with Mars Exploration Rover (MER) Spirit (*Bell et al.*, 2004), identifying meteorites on Mars with MERs Spirit and Opportunity (*Schröder et al.*, 2008), water-ice abundance with Phoenix (*Gyalay et al.*, 2019), and resolving cm-scale gypsum veins in host rocks (*Vaniman et al.*, 2014).

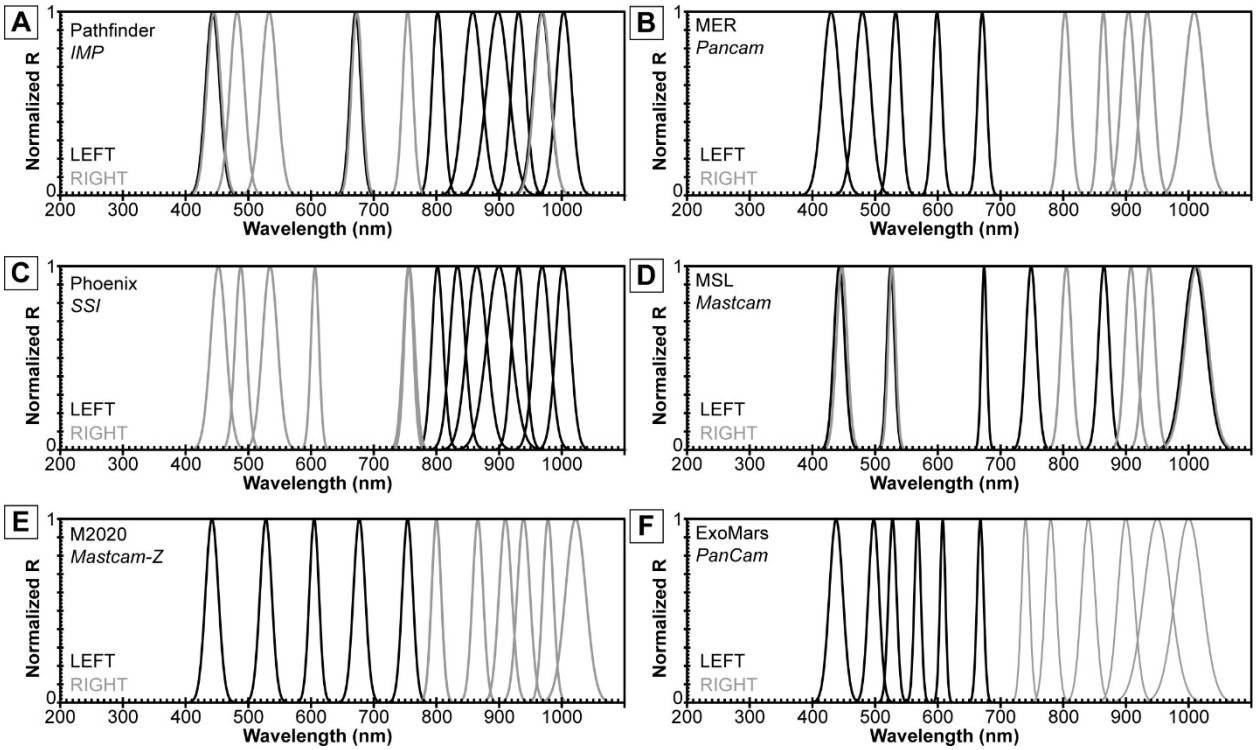

Figure 1. *Geology filter positions and bandwidths for different Mars rover camera instruments. (A) Imager for Pathfinder (IMP) (Smith et al., 1997). (B) Mars Exploration Rover (MER) Pancam (Bell III et al., 2003). (C) Phoenix Surface Stereo Imager (SSI) (Smith et al., 2008). (D) Mars Science Laboratory (MSL) Mastcam (Malin et al., 2017). (E) Mars2020 (M2020) Mastcam-Z (Bell et al., 2021). (F) ExoMars Panoramic Camera (PanCam) (Coates et al., 2017).*

The general filter positions of these multispectral instruments are similar, concentrating on wavelengths that attempt to maximize spectral discrimination of the surface. At the VNIR wavelengths covered by these instruments, the most dominant absorption features are typically due to the presence of iron in different minerals (e.g. *Horgan et al.*, 2014), including: crystal field absorptions near 900 and 1000 nm in the Fe-bearing neo- and inosilicates olivine and pyroxene respectively (e.g. *Cloutis and Gaffey*, 1991), charge transfer and crystal field transitions around 500 and 900 nm in Fe^{3+} oxides such as hematite (e.g. *Townsend*, 1987), and charge transfer effects in iron oxides and hydroxides such as goethite between 400 and 500 nm (e.g. *Morris et al.*, 1985). However, subtle differences between the filter positions and bandwidths across instruments (Figure 1) makes cross-instrument comparisons difficult (*Cousins et al.*, 2012). For example, the longer wavelengths covered by the Mars2020 (M2020) Perseverance rover Mastcam-Z instrument (*Bell et al.*, 2021), allow key absorption features to be identified at and slightly beyond 1000 nm. This spectral region

is of particular interest in studies of hydrated and hydroxylated minerals, due to a weak H_2O overtone absorption near 1000 nm (e.g. *Rice et al.*, 2013b). The differences in filter choices also renders cross-site comparisons more difficult, as the relative capability of instruments in identifying certain mineral groups could result in mis- or non-identification. This effect is particularly important when attempting to compare local in situ studies to infer regional or global processes and geologic histories.

In order to better understand the multispectral performance of the most recent instruments on Mars rovers, and to optimize the future performance of the ExoMars Rosalind Franklin rover, we have carried out an analysis of the spectral performance of three different instruments. We focus this study on Mars Science Laboratory (MSL) Mastcam *(Malin et al., 2017)*, Mars2020 (M2020) Perseverance rover Mastcam-Z (*Bell et al.*, 2021), and ExoMars (EM) Rosalind Franklin Panoramic Camera (PanCam) Wide Angle Camera (WAC) *(Coates et al., 2017)* instruments. Using both laboratory spectral libraries of pure mineral and mixed rock spectra, and hyperspectral data collected from Mars orbit, we determine the error between the multispectral instruments and hyperspectral data. We use these errors to assess the relative performance of these three instruments across a range of mineral types and distinct units on Mars, and discuss confidence levels in comparison across instruments. In comparison to previous studies (e.g. *Cuadros et al.*, 2022), we focus our discussion on the implications for optimization of the EM PanCam instrument, particularly the potential compositions expected at the landing site in Oxia Planum, before arrival at Mars in 2023.

2. Data and Methods

Our approach for determining the spectral performance of a filter set, and thus a rover camera instrument, is similar across different data sets. We first describe the data and pre-processing steps, before outlining the methods used in each case.

2.1 Data

We used the Western Washington University Visible and Infrared Spectroscopy brOwseR (VISOR, *Million et al.* (2022)), a compilation of four open databases (USGS, *Kokaly et al.* (2017); 'playa evaporites', *Crowley* (1991); ASTER / ECOSTRESS, *Meerdink et al.* (2019), *Baldridge et al.* (2009)), to provide spectral library data. We selected a total of 163 spectra across 6 different mineralogical and rock groups (Table S1): basalt ($n = 41$), basaltic soil ($n = 6$), hematite ($n = 35$), olivine ($n = 56$), saponite ($n = 15$), and vermiculite ($n = 10$). These groups were selected due to their relevance and likely occurrence at the Oxia Planum landing site (*Mandon et al.*, 2021; *Quantin-Nataf et al.*, 2021). To predict the spectral response of each instrument to different mineral groups, we first linearly interpolated the VISOR spectra to a 1 nm spectral interval, to allow for detailed comparison (see Section 2.2). We then used the relevant instrument filter center wavelength and bandwidth (Table 1) to spectrally resample all VISOR spectra (Figure 2).

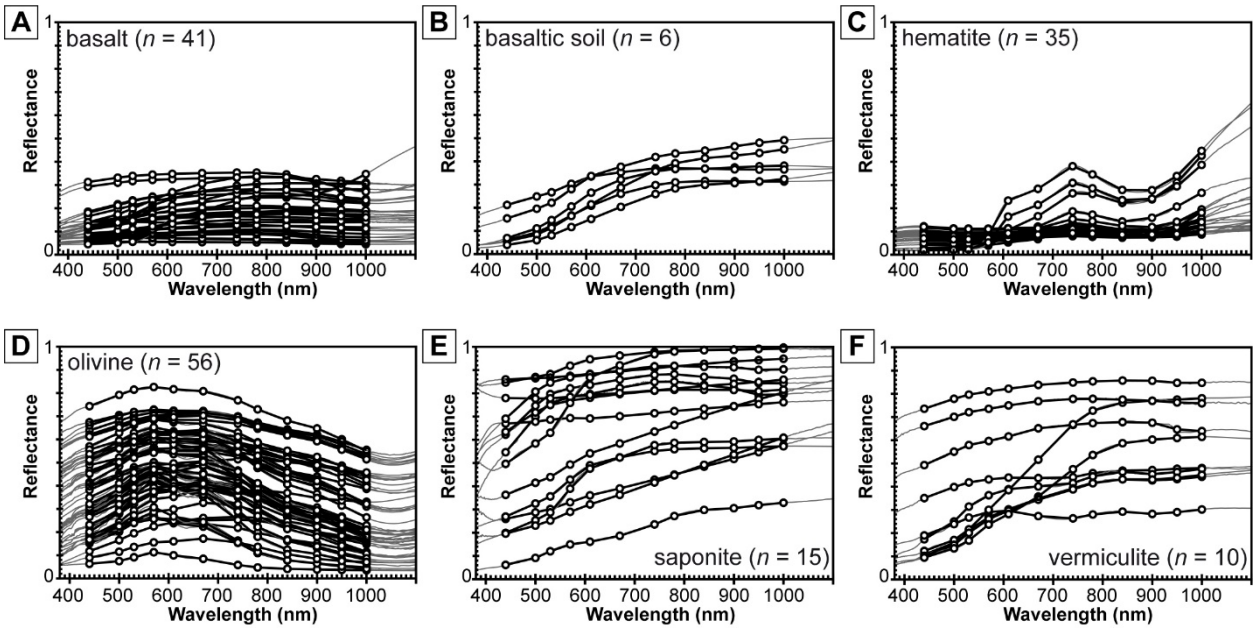

Figure 2. *Spectral resampling of VISOR for PanCam. In each case, the original spectral library spectrum is plotted (thin grey line), in addition to the PanCam spectrally resampled spectrum (thick black line) and filter positions (circles). A total of 163 spectra were used. (A) basalt spectra, (B) basaltic soil, (C), hematite, (D) olivine, (E) saponite, and (F) vermiculite.*

We processed and analyzed Full Resolution Targeted (FRT) Compact Reconnaissance Imaging Spectrometer for Mars (CRISM, (*Murchie et al.*, 2007)) data sets (Table 2), following well-validated techniques (e.g. *Ehlmann et al.*, 2009; *Murchie et al.*, 2009a). We first used a CRISM image of the Vera Rubin Ridge (VRR) area of Gale Crater, explored by the Mars Science Laboratory (MSL, *Grotzinger et al.* (2012)) Curiosity Rover, because of the extensive recent Mastcam multispectral and comparative CRISM studies (*Fraeman et al.*, 2020; *Horgan et al.*, 2020; *Salvatore et al.*, 2020). We then extended our analysis to two further CRISM images at both Oxia Planum and Jezero Crater, the landing sites for ExoMars 2022 Rosalind Franklin rover and Mars 2020 Perseverance rover. All CRISM images were obtained as Map-Projected Targeted Reduced Data Records (MTRDRs) from the NASA Planetary Data System (PDS) Geosciences Node. We used the CRISM Analysis Toolkit (CAT) v7.3 plug-in for the commercial software ENVI to analyze CRISM data when necessary, according to methods described by the CRISM team (*Seelos et al.*, 2011), but no pre-processing or calibration is required for the higher level MTRDR data products. Single pixel spectra were taken from regions of interest (ROIs), as well as from spectrally-bland regions to produce ratioed spectra that emphasize spectral shape. We linearly interpolated the instrument spectra to match the spectral bands of CRISM data. Spectral parameters were also used (e.g. *Vi-*

viano-Beck et al., 2014) to create band threshold ROIs, which were then used to extract multi-pixel spectra.

2.2 Methods

To provide a quantitative and objective measure of how well a filter set captures the spectral morphology, we followed previous studies in assessing the performance of different filter sets by determining the error between full spectra and deconvolved instrument spectra (*Cousins et al.*, 2010; *Cousins et al.*, 2012). We used the Root Mean Square Error (RMSE) method, a common metric to measure the difference between spectra (e.g. *Harris and Grindrod*, 2018). For the spectral library study, the RMSE is between the resampled, interpolated reflectance at filter wavelengths and the original VISOR spectrum,

$$RMSE = \sqrt{\frac{\sum_{\lambda=440}^{1000}[R_m(\lambda)-R_e(\lambda)]^2}{n}} \quad (1)$$

where $R_m( )$ is the reflectance of the mineral spectrum m at wavelength l, $R_e( )$ is the resampled and interpolated reflectance at wavelength l, and n is the number of data points. This procedure is repeated for every VISOR spectrum and instrument filter set. We also separately determine the magnitude of the reflectance error for each filter and instrument, by calculating the difference between every VISOR spectrum and the resampled, interpolated reflectance at each filter wavelength. For the CRISM study, the RMSE is between the resampled, interpolated reflectance at filter wavelengths and the original CRISM spectrum, and is also given by Equation 1. In this case, we calculate a RMSE value for every pixel in the CRISM image array, allowing additional spatial analysis.

3. Results

We separate our results into two main categories, based on laboratory spectral libraries and hyperspectral Mars data, but in each case aim to assess instrument performance for different mineral or rock types.

3.1 Laboratory Spectral Libraries

We first assessed individual instrument performance for all laboratory spectra according to compositional group (Figure 3, Table 3). For EM PanCam, the mean and maximum RMSE across all compositional groups is 0.0022 and 0.0089 respectively. Across the compositional groups of basalt, basaltic soil, hematite, olivine, saponite, and vermiculite, the mean and standard deviation (SD) RMSE values for EM PanCam are 0.0006 (0.0005), 0.0013 (0.0003), 0.0015 (0.0015), 0.0037 (0.0020), 0.0020 (0.0013), and 0.0027 (0.0009) respectively. For MSL Mastcam, the mean and maximum RMSE across all compositional groups is 0.0052 and 0.0250 respectively. Across the compositional groups of basalt, basaltic soil, hematite, olivine, saponite, and vermiculite, the mean and standard deviation (SD) RMSE values for MSL Mastcam are 0.0023 (0.0016), 0.0054 (0.0028), 0.0028 (0.0034), 0.0082 (0.0046), 0.0069 (0.0070), and 0.0067 (0.0036) respectively. For M2020 Mastcam-Z, the mean and maximum RMSE across

all compositional groups is 0.0035 and 0.0172 respectively. Across the compositional groups of basalt, basaltic soil, hematite, olivine, saponite, and vermiculite, the mean and standard deviation (SD) RMSE values for M2020 Mastcam-Z are 0.0010 (0.0008), 0.0024 (0.0007), 0.0025 (0.0031), 0.0061 (0.0036), 0.0026 (0.0017), and 0.0042 (0.0018) respectively. Overall, EM PanCam has the lowest RMSE values, with MSL Mastcam having the largest RMSE values. But there is significant variation between and within each compositional group for each instrument. All instruments show the lowest range of RMSE values for basalt and basaltic soil spectra. The standard deviation of RMSE shows the range in instrument performance for each compositional group, with the largest SD values for EM PanCam being for hematite, for MSL Mastcam being for olivine, and for M2020 Mastcam-Z being for olivine.

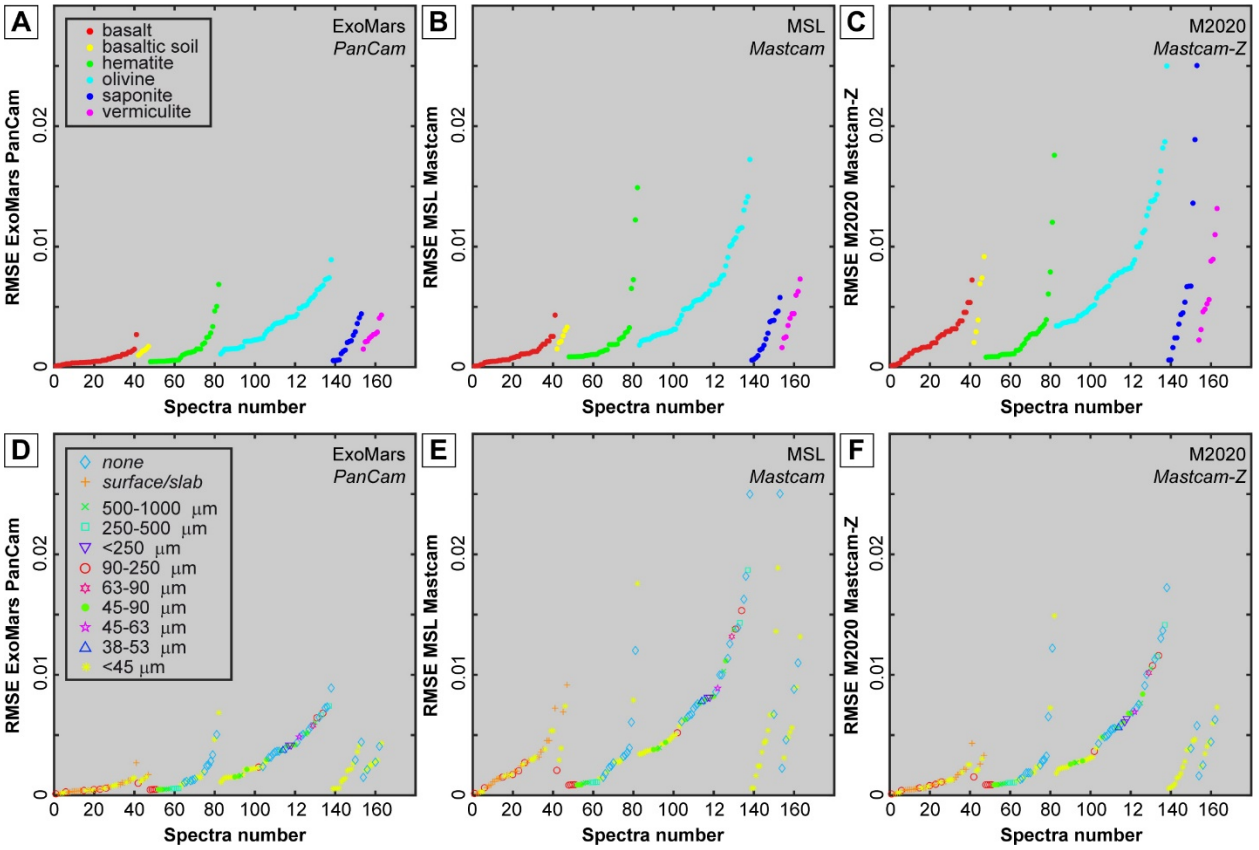

Figure 3. *The Root Mean Square Error (RMSE) for all spectra. In the top row, the spectra are split into compositional group, and retain the same spectra number across plots. (A) RMSE for PanCam. (B) RMSE for Mastcam. (C) RMSE for Mastcam-Z. In the bottom row, the spectra are split into groups according to grain size, as recorded in the spectral library, and retain the same space number across plots. (D) RMSE for PanCam. (E) RMSE for Mastcam. (F) RMSE for*

Mastcam-Z.

We then assessed the relative instrument performance for individual laboratory spectra according to compositional group (Figure 4). EM PanCam has lower RMSE than MSL Mastcam for 137 of 163 spectra, equivalent to 84% of the spectral library. The mean difference in RMSE for those spectra for which EM PanCam has a lower value is 0.0039, whereas for those spectral for which MSL Mastcam has a lower value is 0.0013. Of those 26 spectra for which EM PanCam has higher RMSE, 8 are basalt, 7 are hematite, 9 are olivine, and 2 are saponite. EM PanCam has lower RMSE than M2020 Mastcam-Z for 123 of 163 spectra, equivalent to 75% of the spectral library. The mean difference in RMSE for those spectra for which EM PanCam has a lower value is 0.0022, whereas for those spectral for which M2020 Mastcam-Z has a lower value is 0.0014. Of those 40 spectra for which EM PanCam has higher RMSE, 10 are basalt, 9 are hematite, 13 are olivine, 4 are saponite, and 4 are vermiculite. M2020 Mastcam-Z has lower RMSE than MSL Mastcam for 154 of 163 spectra, equivalent to 94% of the spectral library. The mean difference in RMSE for those spectra for which M2020 Mastcam-Z has a lower value is 0.0019, whereas for those spectral for which MSL Mastcam has a lower value is 0.00009. Of those 9 spectra for which M2020 Mastcam-Z has higher RMSE, 7 are hematite, and 1 is saponite. There does not appear to be any systematic trend in RMSE between EM PanCam and other instruments, but there is a noticeable relationship for RMSE of spectra between MSL Mastcam and M2020 Mastcam-Z. We also assessed the relative instrument performance for individual laboratory spectra according to grain size of the samples (Figure 4). Overall, for those samples in the spectral library for which it is recorded, we see no clear relationships between grain size and RMSE. To some extent, the grain size of a particular compositional group can be limited to just a few ranges, but does not show any correlation with RMSE. In essence, all grain sizes occur at all RMSE values across compositional groups and instruments.

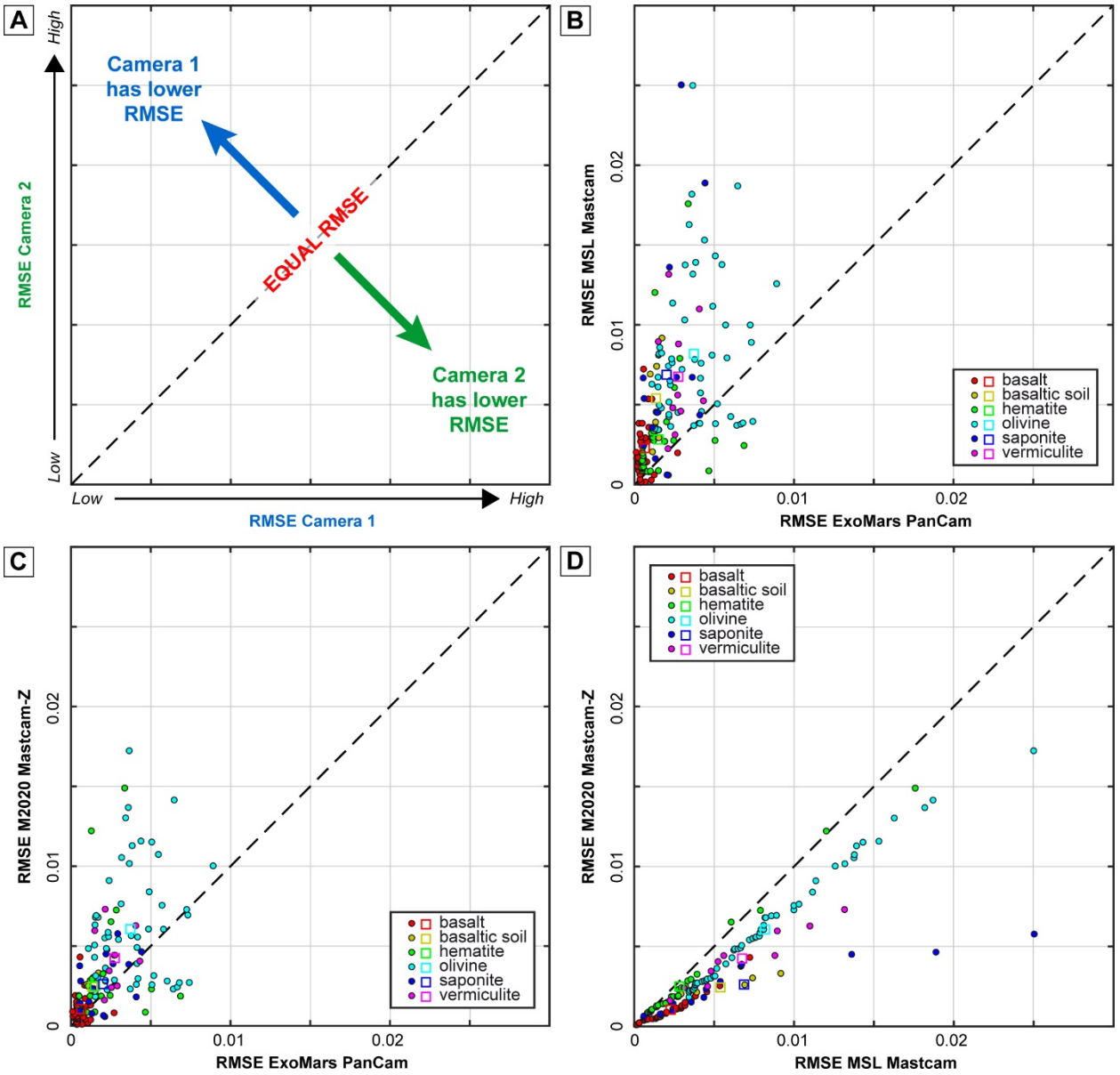

Figure 4. *Comparison of RMSE between instruments. (A) Schematic explanation of which camera has lower RMSE. (B) Bivariate plot of PanCam and Mastcam RMSE. (C) Bivariate plot of PanCam and Mastcam-Z RMSE. (D) Bivariate plot of Mastcam and Mastcam-Z RMSE.*

In an attempt to further explore the performance of different instruments, we assessed the error at each filter wavelength position (Figure 5). In this case, the error was calculated at each wavelength position, rather than as a total RMSE

value. For each instrument, increasing filter number corresponds to increasing wavelength (Table 1). In general, individual filter performance varies within, and across, instruments for different mineral groups, but the lowest errors occur for basalt, basaltic soil, and hematite. For basalt spectra, all instruments have an overall similar performance, tending to have higher errors at the two lowest and highest filter positions, and lowest errors for the middle 7 to 8 filters. For basaltic soil spectra, all instruments have relatively higher errors in the second filter position (and beyond for MSL Mastcam), where there is a generally positive spectral slope in these compositions. For hematite, relative performance of each instrument varies across the filters, with EM PanCam having lowest errors at the smallest filter positions. For olivine spectra, all instruments perform best at filters 6 to 10, but with significant variation across instruments elsewhere. For both saponite and vermiculite, although errors are overall relatively low for EM PanCam, it is noticeable that significant errors occur at the filter 11 position, which has a lower wavelength (950 nm) than both MSL Mastcam (1012 nm) and M2020 Mastcam-Z (978 nm).

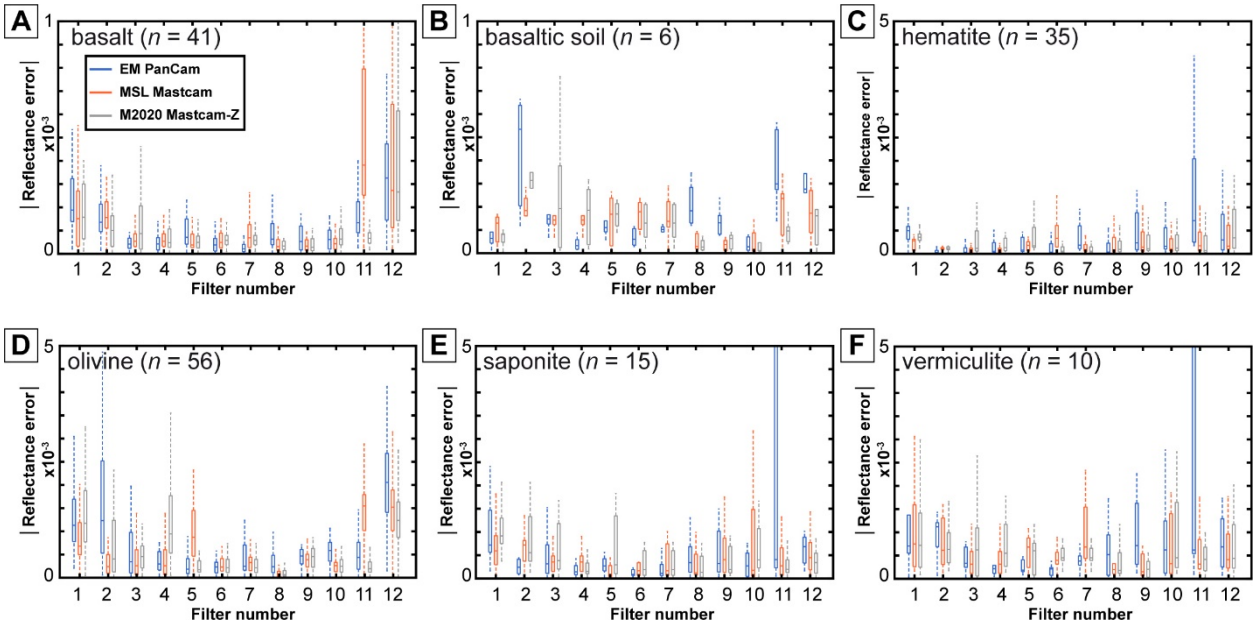

Figure 5. *Box and whisker plot showing absolute reflectance error as a function of filter number. In each case the median (horizontal line), the 25th and 75th percentiles (box), and the most extreme data points not considered outliers – values 1.5 times larger than the interquartile range – (whiskers) are given. A total of 163 spectra were used. (A) basalt spectra, (B) basaltic soil, (C), hematite, (D) olivine, (E) saponite, and (F) vermiculite.*

3.2 Orbital Hyperspectral Data

In using orbital hyperspectral data in our study, we first carried out single

pixel analysis, before moving onto larger multi-pixel regions of interest, and finally whole image examinations. We first focused our attention on the Vera Rubin Ridge area of Gale Crater (Figure 6), which was explored by MSL in 2017 and 2018, the investigation of which included a dedicated multispectral campaign with Mastcam (e.g. *Bennett et al.*, 2021; *Edgar et al.*, 2020; *Fraeman et al.*, 2020; *Horgan et al.*, 2020). To the best of our ability, we identified the area in CRISM hyperspectral data that was explored with Mastcam by MSL, as a ground-truth to our simulations. This particular part of Vera Rubin Ridge has been shown to be rich in hematite, both with Mastcam (*Fraeman et al.*, 2020; *Horgan et al.*, 2020) and other instruments (e.g. *Berger et al.*, 2020; *L'Haridon et al.*, 2020), and is surrounded down- and up-section by rocks containing phyllosilicates and hydrated sulfates respectively (e.g. *Fraeman et al.*, 2016; *Golombek et al.*, 2012; *Milliken et al.*, 2010; *Sheppard et al.*, 2021). All simulated multispectral instruments have a similar overall spectral slope to that seen in the full spectral resolution CRISM data, but with some noticeable differences. To identify and enhance these differences, we used ratioed spectra, applying the common technique of using a spectrally-bland region to remove the background spectral signatures (e.g. *Murchie et al.*, 2009b). The diagnostic absorption feature for hematite at ~850-900 nm is identified in all instruments, but only M2020 Mastcam-Z partially resolves a possible drop in reflectance ~1000 nm. EM PanCam also misidentifies an absorption feature at 670 nm, which is likely the result of the 610 nm filter coinciding with a possible high noise part of the CRISM spectrum. M2020 Mastcam-Z also has a slight decrease in reflectance at that wavelength, but to a lesser degree than EM PanCam.

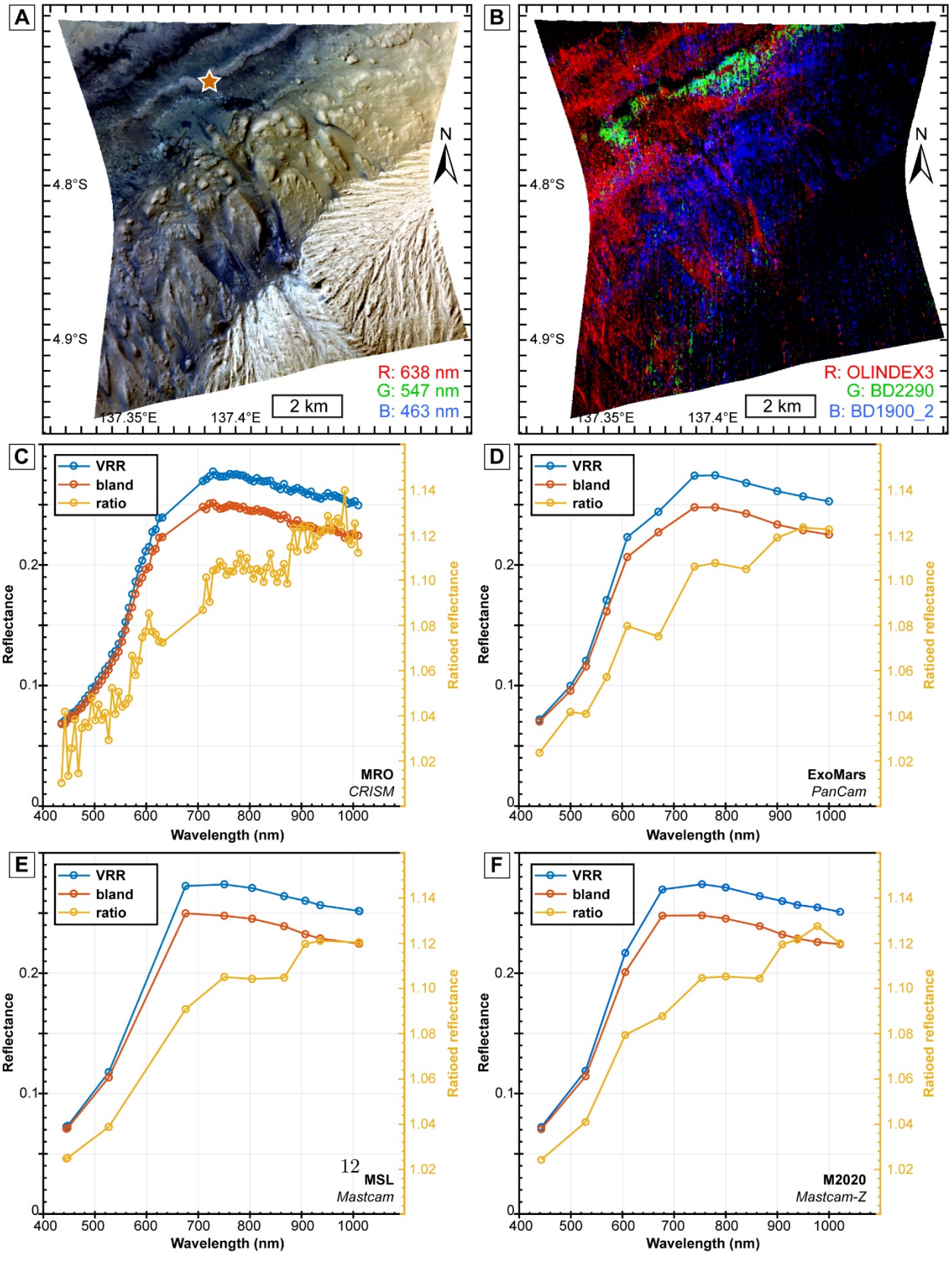
A
B
N
4.8°S
4.9°S
137.35°E
137.4°E
2 km
R: 638 nm
G: 547 nm
B: 463 nm
R: OLINDEX3
G: BD2290
B: BD1900_2
C
D
E
F
VRR
bland
ratio
Reflectance
Ratioed reflectance
Wavelength (nm)
MRO
CRISM
ExoMars
PanCam
MSL
Mastcam
M2020
Mastcam-Z

Figure 6. *Single pixel investigation of spectral resampling of CRISM data for Gale Crater. (A) Visible wavelength RGB image of CRISM hyperspectral cube FRT0000B6F1. Star shows the location of spectrum at Vera Rubin Ridge (VRR) analysed in sub-figures. (B) Spectral parameter image highlighting regions of possible enrichments in different minerals. (C) CRISM single pixel spectra of VRR, bland region, and subsequent ratio. (D) PanCam resampled single pixel spectra of VRR, bland region, and subsequent ratio. (E) Mastcam resampled single pixel spectra of VRR, bland region, and subsequent ratio. (F) Mastcam-Z resampled single pixel spectra of VRR, bland region, and subsequent ratio.*

We next investigated the spectral performance of the instruments using multi-pixel Regions of Interest (ROIs) throughout the CRISM image scene (Figure 7). This common technique uses spectral parameters to first identify regions with particular spectral features (e.g. *Pelkey et al.*, 2007; *Viviano-Beck et al.*, 2014), which are then selected to calculate average spectra. The aim of this approach is to determine typical spectra for regions that could correspond to units of similar spectral shape, and ideally, composition. We used two spectral parameters in the first instance, calculated using standard techniques (*Viviano-Beck et al.*, 2014): (1) BD860_2, which measures the band depth of the absorption feature at 860 nm, often diagnostic of crystalline ferric minerals, especially hematite; and (2) BDI1000VIS, which measures the integrated band depth at 1000 nm, often diagnostic of olivine, pyroxene, or Fe-bearing glass. These BD860_2 and BDI1000VIS ROIs returned spectra averaged over 8009 and 30,225 pixels respectively, for which we investigate both the spectral shape and the RMSE of each instrument from the original CRISM data. The spectra of each instrument has a similar overall shape to the original CRISM spectrum, and on the whole recreates well the spectral morphology. There are no obvious absorption features for either ROI, but the gap in filters between ~530 and 670 nm for MSL Mastcam mean that some information on any possible shoulder at ~600 nm is lost. It is clear that in terms of RMSE from the CRISM data, M2020 Mastcam-Z has the best performance, with a mean (SD) value of 0.0030 (0.0003) for BD860_2 and 0.0028 (0.0003) for BDI1000VIS. EM PanCam has slightly higher RMSE, with a mean (SD) value of 0.0035 (0.0004) for BD860_2 and 0.0031 (0.0003) for BDI1000VIS. MSL Mastcam has noticeably higher RMSE, with a mean (SD) value of 0.0065 (0.0006) for BD860_2 and 0.0070 (0.0008) for BDI1000VIS.

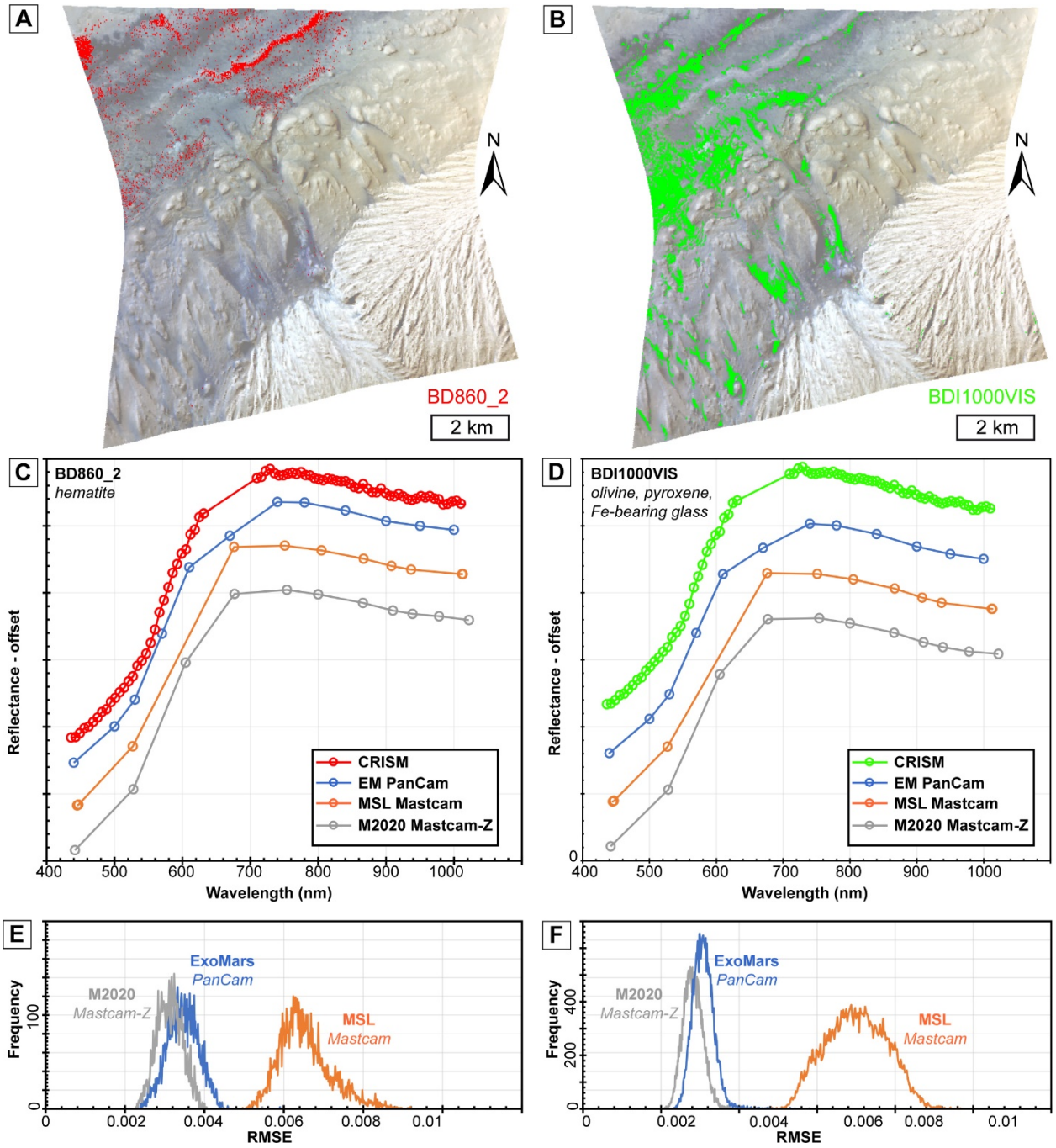

Figure 7. *Multi-pixel region of interest (ROI) investigation of spectral resampling of CRISM data for Gale Crater. (A) Visible wavelength RGB image of*

CRISM hyperspectral cube FRT0000B6F1, overlain by band threshold ROI (8009 pixels) using spectral parameter BD860_2. (B) Visible wavelength RGB image of CRISM hyperspectral cube FRT0000B6F1, overlain by band threshold ROI (30,225 pixels) using spectral parameter BDI1000VIS. (C) Spectra for BD860_2 for CRISM, and resampled for PanCam, Mastcam, and Mastcam-Z. (D) Spectra for BDI1000VIS for CRISM, and resampled for PanCam, Mastcam, and Mastcam-Z. (E) RMSE histogram for BD860_2 between CRISM and resampled for PanCam, Mastcam, and Mastcam-Z. (F) RMSE histogram for BDI1000VIS between CRISM and resampled for PanCam, Mastcam, and Mastcam-Z.

We finally extended the RMSE analysis for the entire CRISM image scene (Figure 8). Again, M2020 has the best performance, with a mean (SD) RMSE value of 0.0037 (0.0007). EM PanCam has only a slightly worse performance, with a mean (SD) RMSE value of 0.0041 (0.0008). MSL Mastcam again has the highest RMSE, with a mean (SD) value of 0.0072 (0.0007) across the entire CRISM image scene. In an attempt to better understand the partial bimodality in the RMSE frequency in EM PanCam data, we further break down the analysis with four more spectral parameters typically used in CRISM analysis. There is a large number of RMSE values that correspond to regions with strong BD640_2 signatures, typical of areas rich in select ferric minerals, especially maghemite. Contributions from other regions that have signatures from SH660_2 (typical of select ferric minerals, especially hematite or goethite), SH770 (typical of select ferric minerals, but less sensitive to low-calcium pyroxene), and BD920 (typical of crystalline ferric minerals and low-calcium pyroxene), are less significant than previous spectral parameters considered, suggesting further contributions not accounted for in the choice of spectral parameters. To investigate where these areas might be in the CRISM image scene, we produced maps of RMSE values, which show high RMSE values that correspond to the higher elevation, anhydrous regions of Mt Sharp (e.g. *Sheppard et al.*, 2021). All instruments show a similar region of high RMSE in this area, but MSL Mastcam also shows additional areas of relatively high RMSE in the west and northwest of the CRISM image scene, corresponding to areas of low RMSE in other instruments.

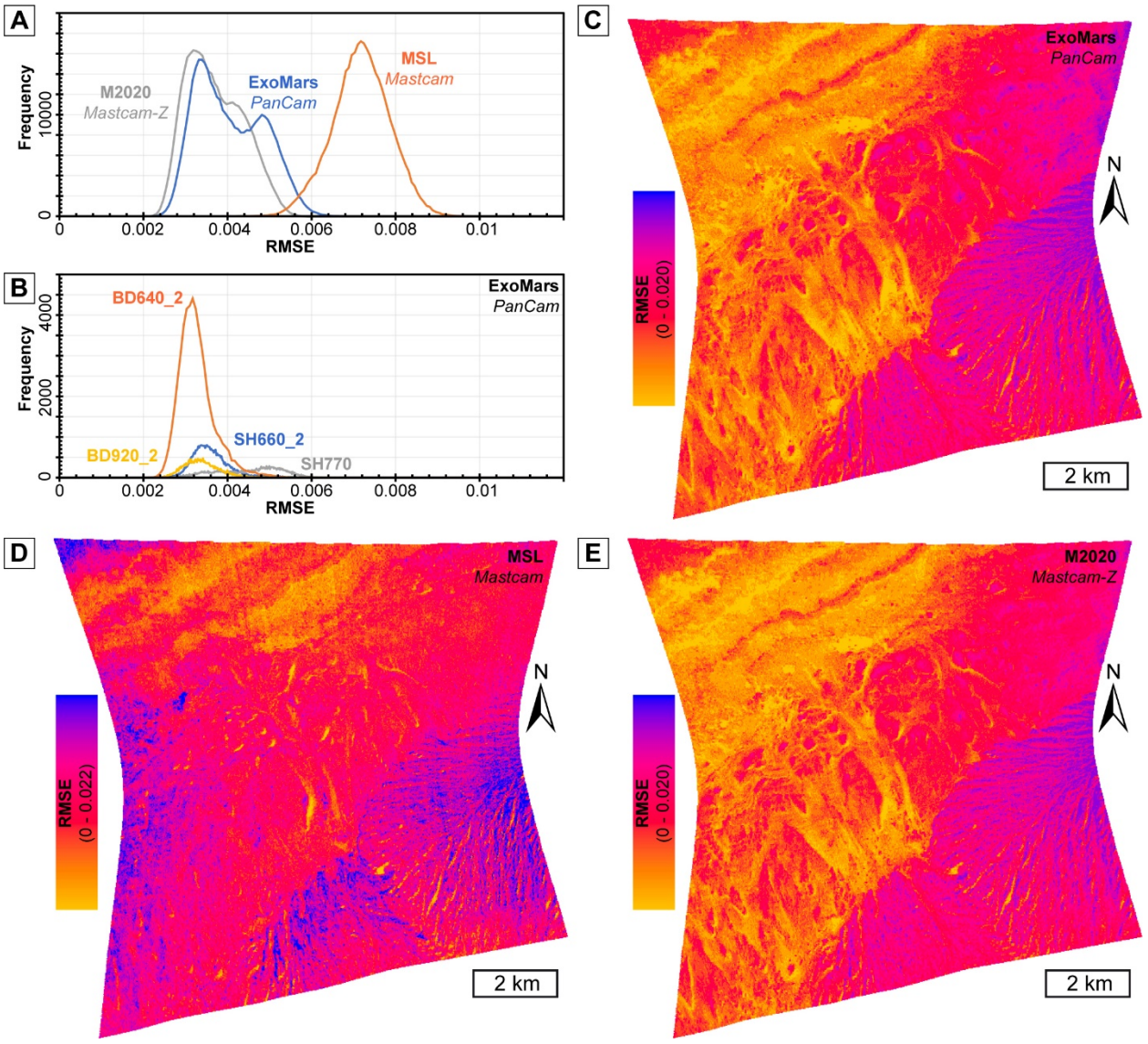

Figure 8. *RMSE analysis for all pixels in CRISM data of Gale Crater. (A) RMSE histogram for all pixels between CRISM and resampled PanCam, Mastcam, and Mastcam-Z. (B) RMSE histogram for ROIs between CRISM and resampled PanCam, using band threshold ROI for spectral parameters BD_640_2 (52,098 pixels), SH660_2 (36,268 pixels), SH770 (27,186 pixels), and BD920_2 (24,404 pixels). (C) RMSE image between CRISM and resampled PanCam. (D) RMSE image between CRISM and resampled Mastcam. (E) RMSE image between CRISM and resampled Mastcam-Z.*

Applying a similar whole CRISM image analysis to four more images, two of the

EM landing site in Oxia Planum, and two of the M2020 landing site in Jezero Crater, yields similar overall results. M2020 Mastcam-Z and EM PanCam have similar RMSE values at all four sites, although EM PanCam has slightly better performance at two of the sites (one in Oxia Planum, one in Jezero Crater). The mean values for these two instruments are similar to those observed at Gale Crater, albeit with no obvious bimodal RMSE distribution. MSL Mastcam has consistently higher RMSE values, with similar values to those observed at Gale Crater. The range of RMSE values is lower at these four sites for all instruments, as demonstrated by the standard deviation of values.

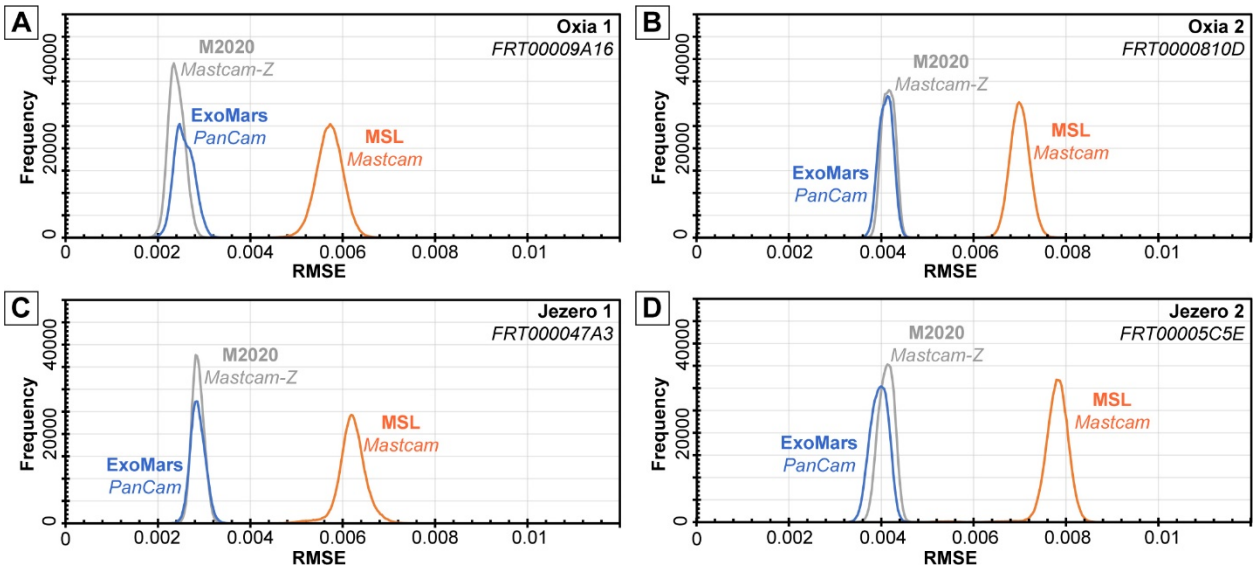

Figure 9. *RMSE analysis for different CRISM images. (A) RMSE histogram for all pixels between CRISM and resampled PanCam, Mastcam, and Mastcam-Z for Oxia Planum site 1 (FRT00009A16). (B) RMSE histogram for all pixels between CRISM and resampled PanCam, Mastcam, and Mastcam-Z for Oxia Planum site 2 (FRT0000810D). (C) RMSE histogram for all pixels between CRISM and resampled PanCam, Mastcam, and Mastcam-Z for Jezero crater site 1 (FRT000047A3). (D) RMSE histogram for all pixels between CRISM and resampled PanCam, Mastcam, and Mastcam-Z for Jezero crater site 2 (FRT00005C5E).*

4. Discussion

The delay in the launch of the EM Rosalind Franklin rover mission means that we can use experience from previous and ongoing multispectral imaging instruments to optimize not only the science returned from the PanCam instrument, but also operational strategies. Although the Mastcam-Z instrument is now on Mars, at the time of writing, initial results have only just begun to be published (*Mangold et al.*, 2021). Thus, relevant examples of the application of in situ multispectral investigations are best provided at present by the Mastcam

instrument (e.g. *Bell et al.*, 2019; *Horton et al.*, 2021; *Johnson et al.*, 2016; *Wellington et al.*, 2017).

In both the laboratory spectral library and CRISM hyperspectral simulations, we have observed similar performance across instruments. Overall, M2020 Mastcam-Z and EM PanCam have similar performance, with both being better than MSL Mastcam in terms of minimizing RMSE. There is a clear systematic improvement in M2020 Mastcam-Z over MSL Mastcam when comparing individual mineral and rock type spectra. This improvement is likely due to the method by which the M2020 Mastcam-Z filters were selected. The intentional repositioning of several narrowband filters on Mastcam-Z was designed to give an overall similar, albeit improved, performance over MSL Mastcam, particularly with hydrated and iron-bearing mineral phases (*Bell et al.*, 2021).

It is important to note that spectral libraries were chosen to reflect the mineralogy expected at the Oxia Planum landing site for the EM Rosalind Franklin rover, and although there are likely to be similarities in composition, the simulated instrument performance may differ slightly with other general mineralogies. Nonetheless, the general performance across mineral groups are similar across all instruments, with the lowest RMSE values for hematite, basalt, and basaltic soil. Although the median error was the lowest for hematite, there are some noticeable outliers that correspond to those spectra that have the largest shoulder at ~750 nm. Minerals with broader, or absent, absorption features in these visible wavelengths, such as olivine, saponite, and vermiculite have overall larger RMSE values. This difference in performance as a function of compositional group is important when considering the possible different aqueous alteration products often used in targeting and detailed study in situ on Mars (e.g. *Bennett et al.*, 2021; *Edgar et al.*, 2020; *Fraeman et al.*, 2020; *Horgan et al.*, 2020).

During the campaign at Vera Rubin Ridge, MSL Mastcam acquired several full multispectral image datasets of the surface. Observations of brushed rock surfaces in particular revealed strong absorption features at ~860 nm, interpreted to be due to the presence of hematite in significant abundances (*Fraeman et al.*, 2020). Our simulations using CRISM data of the same area are not an exact comparison, due to (1) the difference in spatial resolution between orbital and in situ datasets, (2) the gap in sampling between ~620 and 720 nm, and (3) because the surfaces have not been brushed. But, in our simulated data, this absorption feature is present in all instrument ratioed spectra. The MSL Mastcam spectrum in particular has a similar overall shape similar to that observed in situ at the 'Stranraer' target on Sol 2007 (*Fraeman et al.*, 2020). This target had some of the deepest ferric absorptions along this part of the traverse, and is thought to be the opposite end-member to the nearby 'Oban' target, which is likely rich in grey hematite material (*Fraeman et al.*, 2020). It is not possible to separate these end-members from our simulated spectra, but given that both the diagnostic absorption feature and overall spectral shape are correctly recovered, we are confident that (1) our simulated instrument spectra using CRISM data accurately predict the instrument responses to such a mineralogy, and (2)

that both EM PanCam and M2020 Mastcam-Z should be able to identify similar hematite deposits on the surface of Mars.

The main scientific goal of the ExoMars Rosalind Franklin rover mission is to search for life on Mars (*Vago et al.*, 2017). The PanCam instrument will support this goal through the characterization of the surface as the main remote sensing instrument on the rover. The PanCam WACs studied here provide spectral information between approximately 400 and 1000 nm, and are complemented by the PanCam High Resolution Camera (HRC), which provides focusable, visible wavelength, color images through a Bayer filter (*Coates et al.*, 2017). Other complementary instruments include the Infrared Spectrometer for ExoMars (ISEM) instrument, a mast-mounted spectrometer, which provides point spectra between 1150 and 3300 nm (*Korablev et al.*, 2017), and the Close-Up Imager (CLUPI), a drill-mounted, high-resolution, focusable camera that takes color images with a Foveon detector in the 400 – 700 nm range (*Josset et al.*, 2017). Therefore it is important that any optimization of PanCam is carried out with consideration of these other instruments. For example, we have shown that PanCam performs well in the spectral characterization of hematite, but will almost certainly require longer wavelength information from ISEM for minerals such as olivine, saponite, or vermiculite, for which PanCam has a higher RMSE. These apparent poorer identifications are particularly important at Oxia Planum, where the two main types of bedrock can be split into a (1) Fe/Mg-rich clay, possibly including saponite, and (2) probable olivine-rich deposits as identified by a broad absorption feature at ~1000 nm (*Mandon et al.*, 2021). In these bedrock regions, which are likely to be high priority targets for drilling and sampling, it is likely that complementary instruments, such as ISEM, will be critical for mineral identification. Previous studies have used emulators for studying the performance of PanCam and other ExoMars instruments in the field on Earth (e.g. *Allender et al.*, 2020; *Allender et al.*, 2021; *Harris et al.*, 2015), and we can also use multispectral instrument application on Mars as a guide to best practice use (e.g. *Farrand et al.*, 2008; *Farrand et al.*, 2007; *Farrand et al.*, 2014; *Farrand et al.*, 2006; *Farrand et al.*, 2013; *Rice et al.*, 2010; *Rice et al.*, 2013a). These studies made particular use of spectral parameters, which capture some specified spectral feature (e.g. *Bell III et al.*, 2000; *Pelkey et al.*, 2007; *Viviano-Beck et al.*, 2014), to help indicate broad mineralogical composition, abundance, or grain size fluctuations. We will address the optimization of spectral parameters, and calibrated instrument response of PanCam in another study, but note here that instrument error as a function of filter number suggests that spectral parameter performance is likely to vary according to the reflectance error at each filter wavelength. For example, the relatively poor performance by EM PanCam at filter number 11 (950 nm) for the phyllosilicates saponite and vermiculite should be taken into account when devising and selecting spectral parameters that aim to emphasize any hydration-related absorption features close to 1000 nm.

In an ideal situation, PanCam will be able to collect and return to Earth full multispectral data on a regular basis. However, limits in power, data, and time

are all likely to reduce the occasions on which the full geology filter set can be implemented on Mars (e.g. *Balme et al.*, 2019). In these cases, our analysis suggests that minerals with distinctive absorption features in the VNIR, such as hematite, are well suited to restricted filter selection to target specific spectral features. For example, the performance of PanCam in identifying the ~860 nm absorption feature could be exploited during operations by only using filter numbers 8, 9, and 10, which bracket this region. Although PanCam performs well on basaltic and basaltic soil compositions from laboratory data, when spectra are lacking diagnostic absorption features, such as in the higher elevation, anhydrous regions of Mt Sharp, then multispectral performance decreases, reducing the opportunity for targeted filter use. The tactical decision making in selecting PanCam filter use for considering drill targets will then have to be guided carefully by complementary in situ data such as EM PanCam broadband RGB and HRC (*Coates et al.*, 2017), ISEM (*Korablev et al.*, 2017), and CLUPI (*Josset et al.*, 2017), in addition to orbital data such as CRISM (*Murchie et al.*, 2007), HiRISE (*McEwen et al.*, 2007), and CaSSIS (*Thomas et al.*, 2017).

5. Conclusions.

The ability of a visible and near-infrared multispectral imaging instrument to acquire accurate spectra for in situ Mars science is controlled by the selection of narrowband filters. These instruments not only provide contextual geological information, but through the use of narrowband filters at discrete wavelengths, also allow spectral information of the surface to be gathered at visible and near-infrared wavelengths. The primary use of the multispectral information is to determine composition and putative mineralogy that can be used in isolation, but also allow targeted investigation with other payload instruments. Given that different instruments have subtle differences in filter center wavelengths and bandwidths, and have gone to different locations on Mars, it is difficult to quantitatively assess the relative performance across missions. We have assessed the relative performance of filter sets for three different instruments that are either already, or will soon land, on Mars. By determining the root mean square error (RMSE) between the simulated instrumental spectral response, and both laboratory spectral libraries and Mars orbital hyperspectral data, we have assessed the relative performance across instruments, mineral groups, and spectral parameter surface units. We found that PanCam and Mastcam-Z have generally similar values of RMSE, and are consistently lower than for Mastcam, across both laboratory and remote sensing data sets. The general performance across mineral groups are similar across all instruments, with the lowest RMSE values for hematite, basalt, and basaltic soil. Minerals with broader, or absent, absorption features in these visible wavelengths, such as olivine, saponite, and vermiculite have overall larger RMSE values. Instrument RMSE as a function of filter wavelength and bandwidth suggests that spectral parameters that use lower wavelengths are likely to perform better. Our simulations of the spectral performance of the PanCam instrument will help direct comparisons between cross-mission instrument analyses, and allow the future use of targeted filter selection during ExoMars Rosalind Franklin operations on Mars.

Acknowledgments

PMG, RBS, CRC, and EJA thank the UK Space Agency for support (grant ST/T001747/1). SM acknowledges a UK Science and Technology Facilities Council (STFC) PhD studentship (grant ST/R504961/1). All spectral library data are available at the Western Washington University Visible and Infrared Spectroscopy Browser (https://westernreflectancelab.com/visor/). All CRISM data are available through the NASA PDS Geosciences Node CRISM Archive (https://pds-geosciences.wustl.edu/missions/mro/crism.htm). Our derived spectral library and CRISM data results can be accessed at https://doi.org/10.6084/m9.figshare.18545423.

References

https://doi.org/10.1016/j.icarus.2021.114541

https://doi.org/10.1016/j.rse.2008.11.007

https://doi.org/10.1016/j.pss.2018.12.003

https://doi.org/10.1029/1999JE001060

https://doi.org/10.1029/2003JE002070

https://doi.org/10.1029/2019JE006311

https://doi.org/10.1029/2020JE006536

https://doi.org/10.1016/j.pss.2012.07.009

https://doi.org/10.1029/91JB01714

https://doi.org/10.1016/j.icarus.2021.114704

https://doi.org/10.1029/2008JE003237

https://doi.org/10.1029/2006JE002773

https://doi.org/10.1002/2014JE004641

https://doi.org/10.1029/2005JE002495

https://doi.org/10.1016/j.icarus.2013.04.014

https://doi.org/10.1029/2019JE006294

https://doi.org/10.1016/j.icarus.2019.02.033

https://doi.org/10.1016/j.icarus.2015.02.004

https://doi.org/10.1016/j.icarus.2014.02.031

https://doi.org/10.1029/2019JE006322

https://doi.org/10.1029/2019JE006299

https://doi.org/10.1002/2016EA000252

https://doi.org/10.1016/j.rse.2019.05.015

https://doi.org/10.1029/JB090iB04p03126

https://doi.org/10.1016/j.icarus.2009.03.035

https://doi.org/10.1016/j.icarus.2012.09.021

https://doi.org/10.1029/2020JE006372

https://doi.org/10.1029/2008JE003083

https://doi.org/10.1029/96JE03568

https://doi.org/10.1029/JB092iB02p01441

Allender, E. J., C. R. Cousins, M. D. Gunn, and C. M. Caudill (2020), Multiscale and Multispectral Characterization of Mineralogy with the ExoMars 2020 Rover Remote Sensing Payload, *Earth and Space Science*, *7*(4), e2019EA000692, doi:10.1029/2019ea000692.Allender, E. J., C. R. Cousins, M. D. Gunn, and E. R. Mare (2021), Multiscale spectral discrimination of poorly crystalline and intermixed alteration phases using aerial and ground-based ExoMars rover emulator data, *Icarus*, *367*, 114541, doi:.Baldridge, A. M., S. J. Hook, C. I. Grove, and G. Rivera (2009), The ASTER spectral library version 2.0, *Remote Sensing of Environment*, *113*(4), 711-715, doi:.Balme, M. R., et al. (2019), The 2016 UK Space Agency Mars Utah Rover Field Investigation (MURFI), *Planetary and Space Science*, *165*, 31-56, doi:.Bell III, J. F., et al. (2000), Mineralogic and compositional properties of Martian soil and dust: Results from Mars Pathfinder, *Journal of Geophysical Research: Planets*, *105*(E1), 1721-1755, doi:.Bell III, J. F., et al. (2003), Mars Exploration Rover Athena Panoramic Camera (Pancam) investigation, *Journal of Geophysical Research: Planets*, *108*(E12), doi:.Bell, J. F., W. H. Farrand, J. R. Johnson, K. M. Kinch, M. Lemmon, M. C. Parente, M. S. Rice, and D. Wellington (2019), Compositional and Mineralogic Analyses of Mars Using Multispectral Imaging on the Mars Exploration Rover, Phoenix, and Mars Science Laboratory Missions, in *Remote Compositional Analysis: Techniques for Understanding Spectroscopy, Mineralogy, and Geochemistry of Planetary Surfaces*, edited by J. F. Bell Iii, J. L. Bishop and J. E. Moersch, pp. 513-537, Cambridge University Press, Cambridge, doi:DOI: 10.1017/9781316888872.028.Bell, J. F., et al. (2021), The Mars 2020 Perseverance Rover Mast Camera Zoom (Mastcam-Z) Multispectral, Stereoscopic Imaging Investigation, *Space Science Reviews*, *217*(1), 24, doi:10.1007/s11214-020-00755-x.Bell, J. F., et al. (2004), Pancam Multispectral Imaging Results from the Spirit Rover at Gusev Crater, *Science*, *305*(5685), 800-806, doi:10.1126/science.1100175.Bennett, K. A., et al. (2021), Diagenesis Revealed by Fine-Scale Features at Vera Rubin Ridge, Gale Crater, Mars, *Journal of Geophysical Research: Planets*, *126*(5), e2019JE006311, doi:.Berger, J. A., et al. (2020), Elemental Composition and Chemical Evolution of Geologic Materials in Gale Crater, Mars: APXS Results From Bradbury Landing to the Vera Rubin Ridge, *Journal of Geophysical Research: Planets*, *125*(12), e2020JE006536, doi:.Clark, R. N. (2019), Visible

and Near-Infrared Reflectance Spectroscopy: Field and Airborne Measurements, in *Remote Compositional Analysis: Techniques for Understanding Spectroscopy, Mineralogy, and Geochemistry of Planetary Surfaces*, edited by J. F. Bell Iii, J. L. Bishop and J. E. Moersch, pp. 261-273, Cambridge University Press, Cambridge, doi:DOI: 10.1017/9781316888872.013.Cloutis, E. A., and M. J. Gaffey (1991), Spectral-compositional variations in the constituent minerals of mafic and ultramafic assemblages and remote sensing implications, *Earth, Moon, and Planets*, *53*(1), 11-53, doi:10.1007/BF00116217.Coates, A. J., et al. (2017), The PanCam Instrument for the ExoMars Rover, *Astrobiology*, *17*(6-7), 511-541, doi:10.1089/ast.2016.1548.Cousins, C. R., A. D. Griffiths, I. A. Crawford, B. J. Prosser, M. C. Storrie-Lombardi, L. E. Davis, M. Gunn, A. J. Coates, A. P. Jones, and J. M. Ward (2010), Astrobiological Considerations for the Selection of the Geological Filters on the ExoMars PanCam Instrument, *Astrobiology*, *10*(9), 933-951, doi:10.1089/ast.2010.0517.Cousins, C. R., M. Gunn, B. J. Prosser, D. P. Barnes, I. A. Crawford, A. D. Griffiths, L. E. Davis, and A. J. Coates (2012), Selecting the geology filter wavelengths for the ExoMars Panoramic Camera instrument, *Planetary and Space Science*, *71*(1), 80-100, doi:.Crowley, J. K. (1991), Visible and near-infrared (0.4–2.5 m) reflectance spectra of Playa evaporite minerals, *Journal of Geophysical Research: Solid Earth*, *96*(B10), 16231-16240, doi:.Cuadros, J., J. R. Michalski, J. L. Bishop, C. Mavris, S. Fiore, and V. Dekov (2022), Mars-rover cameras evaluation of laboratory spectra of Fe-bearing Mars analog samples, *Icarus*, *371*, 114704, doi:.Edgar, L. A., et al. (2020), A Lacustrine Paleoenvironment Recorded at Vera RubinRidge, Gale Crater: Overview of the Sedimentology and Stratigraphy Observed by the Mars ScienceLaboratory Curiosity Rover, *Journal of Geophysical Research: Planets*, *125*(3), e2019JE006307, doi:10.1029/2019je006307.Ehlmann, B. L., et al. (2009), Identification of hydrated silicate minerals on Mars using MRO-CRISM: Geologic context near Nili Fossae and implications for aqueous alteration, *Journal of Geophysical Research*, *114*, doi:10.1029/2009je003339.Farrand, W. H., J. F. Bell III, J. R. Johnson, R. E. Arvidson, L. S. Crumpler, J. A. Hurowitz, and C. Schröder (2008), Rock spectral classes observed by the Spirit Rover's Pancam on the Gusev Crater Plains and in the Columbia Hills, *Journal of Geophysical Research: Planets*, *113*(E12), doi:.Farrand, W. H., et al. (2007), Visible and near-infrared multispectral analysis of rocks at Meridiani Planum, Mars, by the Mars Exploration Rover Opportunity, *Journal of Geophysical Research: Planets*, *112*(E6), doi:.Farrand, W. H., J. F. Bell III, J. R. Johnson, M. S. Rice, B. L. Jolliff, and R. E. Arvidson (2014), Observations of rock spectral classes by the Opportunity rover's Pancam on northern Cape York and on Matijevic Hill, Endeavour Crater, Mars, *Journal of Geophysical Research: Planets*, *119*(11), 2349-2369, doi:.Farrand, W. H., J. F. Bell III, J. R. Johnson, S. W. Squyres, J. Soderblom, and D. W. Ming (2006), Spectral variability among rocks in visible and near-infrared multispectral Pancam data collected at Gusev crater: Examinations using spectral mixture analysis and related techniques, *Journal of Geophysical Research: Planets*, *111*(E2), doi:.Farrand, W. H., J. F. Bell, J. R. Johnson, M. S. Rice, and J. A. Hurowitz (2013), VNIR multispectral observa-

tions of rocks at Cape York, Endeavour crater, Mars by the Opportunity rover's Pancam, *Icarus*, *225*(1), 709-725, doi:.Farrand, W. H., E. Merényi, and M. C. Parente (2019), Hyper- and Multispectral Visible and Near-Infrared Imaging Analysis, in *Remote Compositional Analysis: Techniques for Understanding Spectroscopy, Mineralogy, and Geochemistry of Planetary Surfaces*, edited by J. F. Bell Iii, J. L. Bishop and J. E. Moersch, pp. 307-323, Cambridge University Press, Cambridge, doi:DOI: 10.1017/9781316888872.016.Fraeman, A. A., B. L. Ehlmann, R. E. Arvidson, C. S. Edwards, J. P. Grotzinger, R. E. Milliken, D. P. Quinn, and M. S. Rice (2016), The stratigraphy and evolution of lower Mount Sharp from spectral, morphological, and thermophysical orbital data sets, *Journal of Geophysical Research: Planets*, *121*(9), 1713-1736, doi:10.1002/2016je005095.Fraeman, A. A., et al. (2020), Synergistic Ground and Orbital Observations of Iron Oxides on Mt. Sharp and Vera Rubin Ridge, *Journal of Geophysical Research: Planets*, *125*(9), e2019JE006294, doi:.Golombek, M., et al. (2012), Selection of the Mars Science Laboratory Landing Site, *Space Science Reviews*, *170*(1), 641-737, doi:10.1007/s11214-012-9916-y.Grotzinger, J. P., et al. (2012), Mars Science Laboratory Mission and Science Investigation, *Space Science Reviews*, *170*(1), 5-56, doi:10.1007/s11214-012-9892-2.Gunn, M. D., and C. R. Cousins (2016), Mars surface context cameras past, present, and future, *Earth and Space Science*, *3*(4), 144-162, doi:10.1002/2016EA000166.Gyalay, S., E. Z. Noe Dobrea, K. Chu, and K. M. Pitman (2019), Nonlinear spectral mixture modeling to estimate water-ice abundance of martian regolith, *Icarus*, *329*, 79-87, doi:.Harris, J. K., C. R. Cousins, M. Gunn, P. M. Grindrod, D. Barnes, I. A. Crawford, R. E. Cross, and A. J. Coates (2015), Remote detection of past habitability at Mars-analogue hydrothermal alteration terrains using an ExoMars Panoramic Camera emulator, *Icarus*, *252*, 284-300, doi:.Harris, J. K., and P. M. Grindrod (2018), Hapke mixture modeling applied to VNIR spectra of mafic mineral mixtures and shergottites: Implications for quantitative analysis of satellite data, *Meteoritics & Planetary Science*, *53*(6), 1179-1206, doi:doi:10.1111/maps.13065.Horgan, B. H. N., E. A. Cloutis, P. Mann, and J. F. Bell (2014), Near-infrared spectra of ferrous mineral mixtures and methods for their identification in planetary surface spectra, *Icarus*, *234*, 132-154, doi:.Horgan, B. H. N., et al. (2020), Diagenesis of Vera Rubin Ridge, Gale Crater, Mars, From Mastcam Multispectral Images, *Journal of Geophysical Research: Planets*, *125*(11), e2019JE006322, doi:.Horton, P., H. R. Kerner, S. Jacob, E. Cisneros, K. L. Wagstaff, and J. Bell (2021), Integrating Novelty Detection Capabilities with MSL Mastcam Operations to Enhance Data Analysis, arXiv:2103.12815.Johnson, J. R., et al. (2016), Constraints on iron sulfate and iron oxide mineralogy from ChemCam visible/near-infrared reflectance spectroscopy of Mt. Sharp basal units, Gale Crater, Mars, *American Mineralogist*, *101*(7), 1501-1514, doi:10.2138/am-2016-5553.Josset, J.-L., et al. (2017), The Close-Up Imager Onboard the ESA ExoMars Rover: Objectives, Description, Operations, and Science Validation Activities, *Astrobiology*, *17*(6-7), 595-611, doi:10.1089/ast.2016.1546.Kokaly, R. F., et al. (2017), USGS Spectral Library Version 7, *Report Rep. 1035*, 68 pp, Reston, VA.Korablev, O. I., et al. (2017), Infrared Spectrometer for ExoMars:

A Mast-Mounted Instrument for the Rover, *Astrobiology*, *17*(6-7), 542-564, doi:10.1089/ast.2016.1543.L'Haridon, J., et al. (2020), Iron Mobility During Diagenesis at Vera Rubin Ridge, Gale Crater, Mars, *Journal of Geophysical Research: Planets*, *125*(11), e2019JE006299, doi:.Malin, M. C., et al. (2017), The Mars Science Laboratory (MSL) Mast cameras and Descent imager: Investigation and instrument descriptions, *Earth and Space Science*, *4*(8), 506-539, doi:.Mandon, L., et al. (2021), Morphological and Spectral Diversity of the Clay-Bearing Unit at the ExoMars Landing Site Oxia Planum, *Astrobiology*, *21*(4), 464-480, doi:10.1089/ast.2020.2292.Mangold, N., et al. (2021), Perseverance rover reveals an ancient delta-lake system and flood deposits at Jezero crater, Mars, *Science*, *0*(0), eabl4051, doi:doi:10.1126/science.abl4051.McEwen, A. S., et al. (2007), Mars Reconnaissance Orbiter's High Resolution Imaging Science Experiment (HiRISE), *Journal of Geophysical Research: Planets*, *112*(E5), E05S02, doi:10.1029/2005JE002605.Meerdink, S. K., S. J. Hook, D. A. Roberts, and E. A. Abbott (2019), The ECOSTRESS spectral library version 1.0, *Remote Sensing of Environment*, *230*, 111196, doi:.Milliken, R. E., J. P. Grotzinger, and B. J. Thomson (2010), Paleoclimate of Mars as captured by the stratigraphic record in Gale Crater, *Geophysical Research Letters*, *37*(4), n/a-n/a, doi:10.1029/2009gl041870.Million, C. C., M. St. Clair, M. Rice, and A. Vaughan (2022), Software Tools for Rapid Analysis of Mastcam-Z Multispectral Data, in *53rd Lunar and Planetary Science Conference*, edited, Lunar and Planetary Institute, Houston.Morris, R. V., H. V. Lauer Jr., C. A. Lawson, E. K. Gibson Jr., G. A. Nace, and C. Stewart (1985), Spectral and other physicochemical properties of submicron powders of hematite (-Fe2O3), maghemite (-Fe2O3), magnetite (Fe3O4), goethite (-FeOOH), and lepidocrocite (-FeOOH), *Journal of Geophysical Research: Solid Earth*, *90*(B4), 3126-3144, doi:.Murchie, S., et al. (2007), Compact Reconnaissance Imaging Spectrometer for Mars (CRISM) on Mars Reconnaissance Orbiter (MRO), *Journal of Geophysical Research*, *112*(E5), doi:10.1029/2006je002682.Murchie, S. L., et al. (2009a), A synthesis of Martian aqueous mineralogy after 1 Mars year of observations from the Mars Reconnaissance Orbiter, *Journal of Geophysical Research*, *114*, doi:10.1029/2009je003342.Murchie, S. L., et al. (2009b), Compact Reconnaissance Imaging Spectrometer for Mars investigation and data set from the Mars Reconnaissance Orbiter's primary science phase, *Journal of Geophysical Research: Planets*, *114*(E2), doi:10.1029/2009je003344.Mustard, J. F., and T. D. Glotch (2019), Theory of Reflectance and Emittance Spectroscopy of Geologic Materials in the Visible and Infrared Regions, in *Remote Compositional Analysis: Techniques for Understanding Spectroscopy, Mineralogy, and Geochemistry of Planetary Surfaces*, edited by J. F. Bell Iii, J. L. Bishop and J. E. Moersch, pp. 21-41, Cambridge University Press, Cambridge, doi:DOI: 10.1017/9781316888872.004.Pelkey, S. M., et al. (2007), CRISM multispectral summary products: Parameterizing mineral diversity on Mars from reflectance, *Journal of Geophysical Research*, *112*(E8), doi:10.1029/2006je002831.Quantin-Nataf, C., et al. (2021), Oxia Planum: The Landing Site for the ExoMars "Rosalind Franklin" Rover Mission: Geological Context and Prelanding Interpretation, *Astrobiology*, *21*(3), 345-366, doi:10.1089/ast.2019.2191.Rice, M. S.,

J. F. Bell, E. A. Cloutis, A. Wang, S. W. Ruff, M. A. Craig, D. T. Bailey, J. R. Johnson, P. A. de Souza, and W. H. Farrand (2010), Silica-rich deposits and hydrated minerals at Gusev Crater, Mars: Vis-NIR spectral characterization and regional mapping, *Icarus*, *205*(2), 375-395, doi:.Rice, M. S., J. F. Bell, III, R. E. Arvidson, W. H. Farrand, J. R. Johnson, J. W. Rice, S. W. Ruff, S. W. Squyres, and A. Wang (2013a), Mapping Hydration with the Mars Exploration Rover (MER) Pancam Instruments: Recent Results from Opportunity at Endeavour Crater, edited, pp. EGU2013-7035.Rice, M. S., E. A. Cloutis, J. F. Bell, D. L. Bish, B. H. Horgan, S. A. Mertzman, M. A. Craig, R. W. Renaut, B. Gautason, and B. Mountain (2013b), Reflectance spectra diversity of silica-rich materials: Sensitivity to environment and implications for detections on Mars, *Icarus*, *223*(1), 499-533, doi:.Rossman, G. R., and B. L. Ehlmann (2019), Electronic Spectra of Minerals in the Visible and Near-Infrared Regions, in *Remote Compositional Analysis: Techniques for Understanding Spectroscopy, Mineralogy, and Geochemistry of Planetary Surfaces*, edited by J. F. Bell Iii, J. L. Bishop and J. E. Moersch, pp. 3-20, Cambridge University Press, Cambridge, doi:DOI: 10.1017/9781316888872.003.Salvatore, M. R., A. A. Fraeman, P. J. Gasda, E. B. Rampe, T. S. J. Gabriel, O. Gasnault, G. David, L. A. Edgar, and E. Dehouck (2020), Lessons Learned When Reconciling Orbital and In Situ Exploration of Vera Rubin Ridge, Gale Crater, Mars, in *Lunar and Planetary Science Conference*, edited, p. 2714.Schröder, C., et al. (2008), Meteorites on Mars observed with the Mars Exploration Rovers, *Journal of Geophysical Research: Planets*, *113*(E6), doi:doi:10.1029/2007JE002990.Seelos, F. P., S. L. Murchie, D. C. Humm, O. S. Barnouin, F. Morgan, H. W. Taylor, C. Hash, and C. Team (2011), CRISM Data Processing and Analysis Products Update — Calibration, Correction, and Visualization, in *Lunar and Planetary Science Conference*, edited, p. 1438.Sheppard, R. Y., R. E. Milliken, M. Parente, and Y. Itoh (2021), Updated Perspectives and Hypotheses on the Mineralogy of Lower Mt. Sharp, Mars, as Seen From Orbit, *Journal of Geophysical Research: Planets*, *126*(2), e2020JE006372, doi:.Smith, P. H., et al. (2008), Introduction to special section on the Phoenix Mission: Landing Site Characterization Experiments, Mission Overviews, and Expected Science, *Journal of Geophysical Research: Planets*, *113*(E3), doi:.Smith, P. H., et al. (1997), The imager for Mars Pathfinder experiment, *Journal of Geophysical Research: Planets*, *102*(E2), 4003-4025, doi:.Squyres, S. W., et al. (2008), Detection of silica-rich deposits on Mars, *Science*, *320*(5879), 1063-1067, doi:10.1126/science.1155429.Thomas, N., et al. (2017), The Colour and Stereo Surface Imaging System (CaSSIS) for the ExoMars Trace Gas Orbiter, *Space Science Reviews*, *212*(3), 1897-1944, doi:10.1007/s11214-017-0421-1.Townsend, T. E. (1987), Discrimination of iron alteration minerals in visible and near-infrared reflectance data, *Journal of Geophysical Research: Solid Earth*, *92*(B2), 1441-1454, doi:.Vago, J., O. Witasse, H. Svedhem, P. Baglioni, A. Haldemann, G. Gianfiglio, T. Blancquaert, D. McCoy, and R. de Groot (2015), ESA ExoMars program: The next step in exploring Mars, *Solar System Research*, *49*(7), 518-528, doi:10.1134/s0038094615070199.Vago, J. L., et al. (2017), Habitability on Early Mars and the Search for Biosignatures with the ExoMars

Rover, *Astrobiology*, *17*(6-7), 471-510, doi:10.1089/ast.2016.1533.Vaniman, D. T., et al. (2014), Mineralogy of a Mudstone at Yellowknife Bay, Gale Crater, Mars, *Science*, *343*(6169), doi:10.1126/science.1243480.Viviano-Beck, C. E., et al. (2014), Revised CRISM spectral parameters and summary products based on the currently detected mineral diversity on Mars, *Journal of Geophysical Research: Planets*, *119*(6), 1403-1431, doi:doi:10.1002/2014JE004627.Wellington, D. F., J. F. Bell, J. R. Johnson, K. M. Kinch, M. S. Rice, A. Godber, B. Ehlmann, A. Fraeman, and C. Hardgrove (2017), Visible to near-infrared MSL/Mastcam multispectral imaging: Initial results from select high-interest science targets within Gale Crater, Mars, *American Mineralogist*, *102*(6), 1202-1217, doi:10.2138/am-2017-5760CCBY.

Table 1. *Geology filter center wavelength ( ) and Full Width-Half Maximum (FWHM) of multispectral imaging instruments on Mars. Values in parentheses represent an identical filter in a separate left or right camera.*

Filter number	EM PanCam[1]	MSL Mastcam[2]	M2020 Mastcam-Z[3]			
	(nm)	FWHM (nm)	(nm)	FWHM (nm)	(nm)	FWHM (n
1	440	25	445	20	442	24
2	500	20	447	20	528	22
3	530	15	527	14	605	18
4	570	12	(527)	(14)	677	22
5	610	10	676	10	754	20
6	670	12	751	20	800	18
7	740	15	805	20	(800)	(18)
8	780	20	867	20	866	20
9	840	25	908	22	910	24
10	900	30	937	22	939	24
11	950	50	1012	42	978	20
12	1000	50	1013	42	1022	38

[1] *Coates et al.* (2017), [2] *Malin et al.* (2017), [3] *Bell et al.* (2021)

Table 2. *CRISM images used in Mars data simulations.*

CRISM ID	Acquisition Date	Location	Resolution	
			Spectral (nm)	Spatial (m/px)
FRT0000B6F1	2008-07-09	Gale Crater	6.55	18
FRT00009A16	2008-01-25	Oxia Planum	6.55	18
FRT0000810D	2007-10-06	Oxia Planum	6.55	18
FRT000047A3	2007-02-26	Jezero Crater	6.55	18
FRT00005C5E	2007-05-19	Jezero Crater	6.55	18

Table 3. *Instrument performance for all laboratory spectra according to compositional group. In each case, the mean and standard deviation (SD) RMSE are given.*

Compositional group	EM PanCam	MSL Mastcam	M2020 Mastcam-Z			
	Mean	SD	Mean	SD	Mean	SD
All	0.0022	0.0019	0.0052	0.0047	0.0035	0.0034
Basalt	0.0006	0.0005	0.0023	0.0016	0.0010	0.0008
Basaltic soil	0.0013	0.0003	0.0054	0.0028	0.0024	0.0007
Hematite	0.0015	0.0015	0.0028	0.0034	0.0025	0.0031
Olivine	0.0037	0.0020	0.0082	0.0046	0.0061	0.0036
Saponite	0.0020	0.0013	0.0069	0.0070	0.0026	0.0017
Vermiculite	0.0027	0.0009	0.0067	0.0036	0.0042	0.0018